



OPEN

Travertine crystal growth ripples record the hydraulic history of ancient Rome's Anio Novus aqueduct

Duncan Keenan-Jones^{1✉}, Davide Motta^{2✉}, Marcelo H. Garcia³, Mayandi Sivaguru⁴, Mauricio Perillo⁵, Ryan K. Shosted⁶ & Bruce W. Fouke^{3,7,8,9,10}

Travertine crystal growth ripples are used to reconstruct the early hydraulic history of the Anio Novus aqueduct of ancient Rome. These crystalline morphologies deposited within the aqueduct channel record the hydraulic history of gravity-driven turbulent flow at the time of Roman operation. The wavelength, amplitude, and steepness of these travertine crystal growth ripples indicate that large-scale sustained aqueduct flows scaled directly with the thickness of the aqueous viscous sublayer. Resulting critical shear Reynolds numbers are comparable with those reconstructed from heat/mass transfer crystalline ripples formed in other natural and engineered environments. This includes sediment transport in rivers, lakes, and oceans, chemical precipitation and dissolution in caves, and melting and freezing in ice. Where flow depth and perimeter could be reconstructed from the distribution and stratigraphy of the travertine within the Anio Novus aqueduct, flow velocity and rate have been quantified by deriving roughness-flow relationships that are independent of water temperature. More generally, under conditions of near-constant water temperature and kinematic viscosity within the Anio Novus aqueduct channel, the travertine crystal growth ripple wavelengths increased with decreasing flow velocity, indicating that systematic changes took place in flow rate during travertine deposition. This study establishes that travertine crystal growth ripples such as those preserved in the Anio Novus provide a sensitive record of past hydraulic conditions, which can be similarly reconstructed from travertine deposited in other ancient water conveyance and storage systems around the world.

A reliable supply of fresh drinking water, coupled with an effective water delivery management system, are two of the essential elements required to build and maintain human civilization. Fulfilment of these basic requirements has carried power and prestige in virtually every culture throughout human history¹. Where water has sufficiently high supersaturated concentrations of dissolved minerals (hard water), it precipitates deposits composed of calcium carbonate (CaCO₃) limestone called *travertine*^{2,3} within water transport and storage systems. In the process, these travertine deposits preserve a record of the complexly intertwined physical, chemical, and biological processes that have influenced their deposition²⁻⁵. Travertine deposited during the operation

¹School of Historical and Philosophical Inquiry, The University of Queensland, St Lucia, QLD 4072, Australia. ²Department of Mechanical and Construction Engineering, Northumbria University, Wynne Jones Building, Newcastle Upon Tyne NE1 8ST, UK. ³Ven Te Chow Hydrosystems Laboratory, Department of Civil and Environmental Engineering, University of Illinois at Urbana-Champaign, 205 North Mathews Avenue, Urbana, IL 61801, USA. ⁴Cytometry and Microscopy to Omics Facility, Roy J. Carver Biotechnology Center, University of Illinois Urbana-Champaign, 231 Edward L. Madigan Laboratory, 1201 W. Gregory Drive, Urbana, IL 61801, USA. ⁵ExxonMobil Upstream Business Development, 22777 Springwoods Village Parkway, Spring, TX 77389, USA. ⁶Department of Linguistics, University of Illinois at Urbana-Champaign, 707 S Mathews Ave., Urbana, Champaign, IL, USA. ⁷Department of Geology, University of Illinois at Urbana-Champaign, 1301 W. Green St., Urbana, IL 61801, USA. ⁸Department of Evolution, Ecology, and Behavior, University of Illinois at Urbana-Champaign, 505 S. Goodwin Ave., Urbana, IL, USA. ⁹Roy J. Carver Biotechnology Center, University of Illinois at Urbana-Champaign, 1206 W. Gregory Drive, Urbana, IL 61801, USA. ¹⁰Carl R. Woese Institute for Genomic Biology and Carl Zeiss Labs@Location Partner, University of Illinois at Urbana-Champaign, 1206 W. Gregory Drive, Urbana, IL 61801, USA. ✉email: d.keenanjones@uq.edu.au; davide.motta@northumbria.ac.uk

of historical aqueducts has recorded changes in human activity and climate in Europe and the Middle East^{6–15}, Pre-Columbian North America¹⁶, Central Asia¹⁷ and Australia¹⁸. While dominated by CaCO₃ crystals that precipitate directly from the flowing aqueduct water, aqueduct travertine also contains varying but relatively minor amounts of downstream-transported sediments and plant debris¹⁹. This combination of travertine crystallization and sedimentation processes posed a significant ongoing problem for the maintenance of ancient aqueducts²⁰. Travertine had to be regularly removed manually^{19,21,22} to prevent it from becoming too heavy for the aqueduct structural supports, while also increasing wall roughness, narrowing channel cross-sectional area, and reducing the flow capacity²³. As a result of these relationships between aqueduct flow and travertine formation, aqueduct travertine has recently been used to reconstruct flow rates based on their spatial and temporal distribution within the archaeologically significant and protected ruins of the Anio Novus aqueduct at Roma Vecchia, Italy^{23,24}.

In many natural submarine and subaerial environmental systems, downstream transport of sedimentary particles creates sediment transport morphologies called ripples and dunes that have been extensively studied^{25–32}. In addition, other types of deposits called “heat/mass transfer” crystalline deposits have also been described that form ripples as a result of either heat transfer during melting and freezing in ice (e.g. ice ripples)^{33–38}, or mass transfer during mineral precipitation and dissolution in caves (e.g. solution ripples^{36–42}; Supplementary Information S1). Another common example of heat/mass transfer crystalline deposits are travertine microterraces formed in terrestrial spring, river, lake, and cave hydraulic systems. In these environments, travertine microterraces (repeated pond and dam stair-steps) form as a result of complex interactions between crystal precipitation from supersaturated aqueous solutions, changing gravity-dependent low-flow hydraulic regimes, the presence and metabolic activity of microorganisms, and a small amount of downstream sediment transport^{2,43–48}.

The present study evaluates an unexpected new class of well-preserved heat/mass transfer crystalline deposits that formed during travertine precipitation on the floors, walls, and roofs of the main channel of the Anio Novus aqueduct of ancient Rome^{19,23,24}. These deposits were initially reported as “ripples” in the Anio Novus travertine¹⁹ and later called “ripple-like” morphologies in geographically widespread aqueducts in France¹³, Istanbul and Jordan⁹, Germany¹⁵, and Turkey¹⁴. To be consistent with previous literature, the term “ripple” in the present study will be used as a descriptive morphological term, to which modifiers are added to indicate specific compositions and genetic processes of formation and deposition. Examples include “sediment transport ripples”^{28,32}, “solution ripples”⁴², and even “ice ripples”³⁷. Depositional morphologies observed in the present study of Anio Novus aqueduct travertine deposits will therefore be consistently described as “travertine crystal growth ripples”. This terminology confirms that the travertine ripple morphologies form from a process of constructional crystal growth directly from the flowing aqueduct water. Furthermore, this terminology reflects the distinctly different typology of travertine crystallized from complex physical, chemical, and biological mechanisms^{2–5}, which is a fundamentally different process from the fluid mechanics controlling sedimentary transport ripple formation²⁸. At the same time, the nomenclature “travertine crystal growth ripples” recognizes that gravity-driven, open-channel turbulent flow is also influential in convective diffusion during travertine CaCO₃ crystal precipitation³³. As a result, the present study combines analyses of travertine crystal growth ripple morphology, 3D floor and wall distributions within the aqueduct channel, and hydraulic modeling to reconstruct the operating conditions of the ancient Anio Novus aqueduct.

Materials and methods

Archeological setting. The largest and most important addition to the water supply system of ancient Rome was the unprecedented simultaneous building of the Aqua Claudia and the Anio Novus aqueducts between 38 and 52 CE⁴⁹. The 11 aqueducts built in Rome between 312 BCE and 226 CE constituted a larger and more complex urban water supply system than any before it. Collectively, these aqueducts, 500 km in total length⁵⁰, enabled the population density to reach unprecedented levels that rival those of modern-day urbanization⁵¹. Considerable municipal funds were expended in their maintenance and in some cases the aqueducts continued to be used for over a thousand years⁵².

The Anio Novus^{23,24} was the farthest-reaching aqueduct ever built by Imperial Rome, carrying water from the Aniene (Latin: *Anio*) River and one of its tributaries, the *rivus Herculanus*, some 87 km into the Eternal City²¹ (Fig. 1A). The Anio Novus aqueduct was fed from the Middle and Upper Basins of the Aniene River²¹, which flows through and dissolves Mesozoic (Upper Triassic to Upper Cretaceous) CaCO₃ marine limestones comprising the Simbruini Mountains⁵³. Around 98 CE, the water supply system of Rome was thoroughly described in the *De Aquis* compendium by Sextus Julius Frontinus, Rome’s water commissioner (*curator aquarum*). Because of the high carbonate supersaturation of the water, travertine reached more than 1 m in thickness at some sites along the aqueduct system⁴⁹. The Anio Novus was the highest-elevation aqueduct along most of the Aniene valley and the second highest in elevation within the city of Rome itself⁵⁴. Aqueduct elevation was important (Supplementary Information S2) since Roman water supply was predominantly gravity-driven and only areas below an aqueduct could be supplied with any significant volume of water⁵⁰. Maintenance of the Anio Novus apparently ceased sometime between the fifth and eighth centuries CE^{52,55}.

Sample collection for the present study was conducted under research permits granted by the Soprintendenza Speciale per il Colosseo, il Museo Nazionale Romano e l’Area Archeologica di Roma and the Soprintendenza Archeologia, Belle Arti e Paesaggio per l’Area Metropolitana di Roma, la Provincia di Viterbo e l’Etruria Meridionale. Aqueduct travertine samples were collected from three sites: (1) the underground Galleria Egidio section of the Tivoli Loop²³ (Fig. 1A); (2) the Empiglione Bridge section on the Tivoli Bypass (Figs. 1A and 2); and (3) three locations within the site of Roma Vecchia²⁴ (Fig. 1B). Travertine deposited at each of these three locations lined the channel floor, walls and sometimes roof of the Anio Novus aqueduct, exhibiting depositional characteristics that are generally consistent with previous descriptions from other Roman aqueduct systems^{6,7,9,15}.

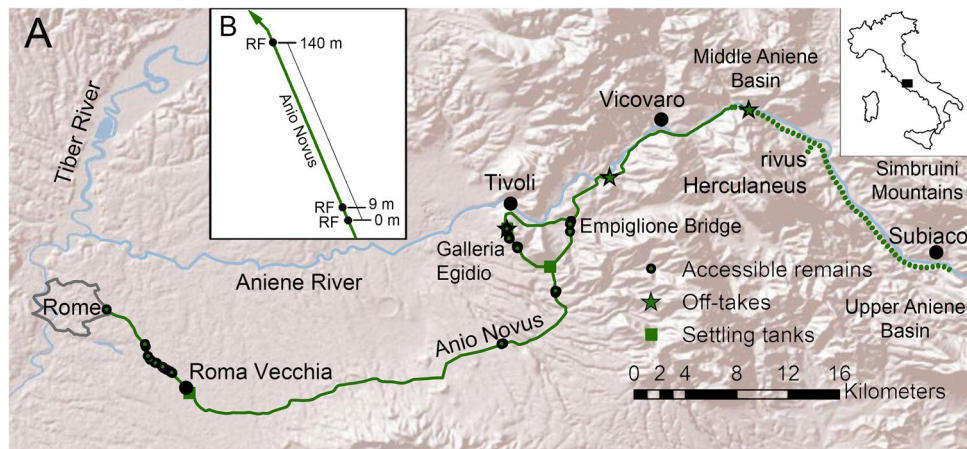


Figure 1. (A) Route of the Anio Novus aqueduct from Subiaco in the Apennines into Rome. Geographic location of the Galleria Egidio, Empiglione Bridge and Roma Vecchia sites are indicated. (B) Enlargement of the Anio Novus aqueduct channel at Roma Vecchia showing relative locations of the upstream (RF 0 m), intermediate (RF 9 m), and downstream (RF 140 m) sample collection locations. Modified from Keenan-Jones et al.²⁴.

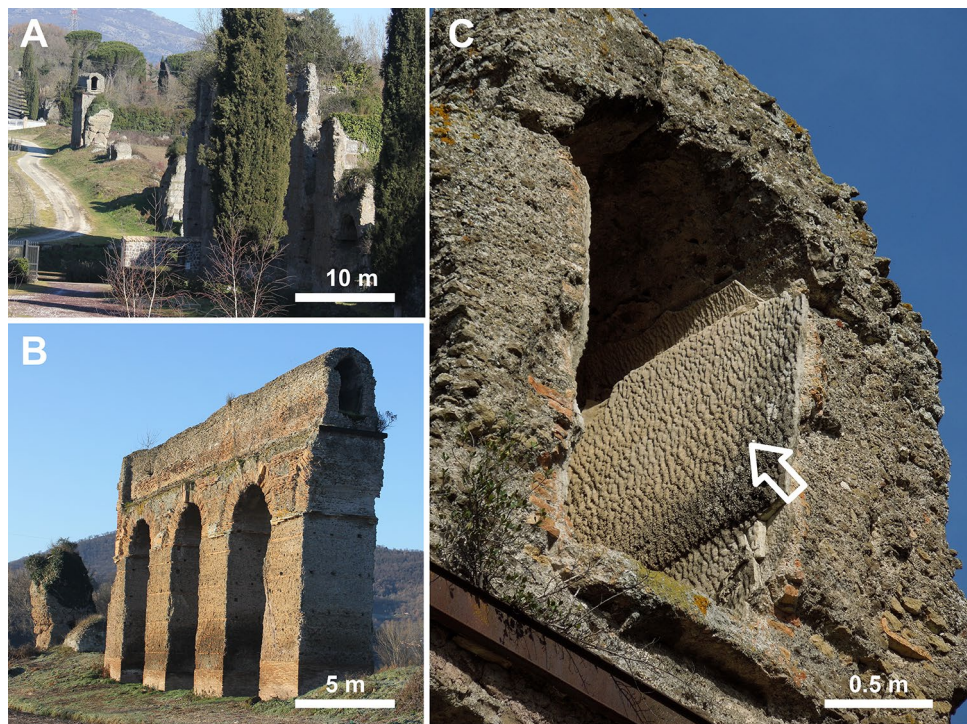


Figure 2. Field photographs of the Anio Novus aqueduct at Empiglione Bridge on the Tivoli Bypass (location shown in Fig. 1A). (A) Empiglione Bridge looking upstream. (B) Closeup of arcade at upstream end (top left) of (A), now looking downstream. (C) Travertine crystal growth ripples (white arrow) on the downstream vertical side wall of the arcade shown in (B) (looking upstream). This opening is visible in the top left of (A).

The distribution and depositional characteristics of the travertine crystal growth ripples at the Galleria Egidio and Roma Vecchia sites were used to justify the assumption of uniform flow within the Anio Novus aqueduct at these locations, which have been previously presented in detail^{23,24} (Supplementary Table S2, Supplementary Information S5.1). Similarly, the Empiglione Bridge site, which begins at the Anio Novus' channel bifurcation around Tivoli (Fig. 1A), contains a 625 m-long bridge⁵⁵ that also provides strong evidence for uniform flow. This is because it crossed the valley of the Empiglione River by means of a straight arcade that maintained essentially constant gradients and cross-sectional geometries^{49,54}. The Empiglione Bridge sample sites in the present study

were located ~200 m downstream of the bifurcation and 400 m upstream of the end of the bridge (Fig. 2). The only known aqueduct junction on the bridge is an offtake to a cistern located 230 m downstream of the measured cross section, which is not expected to have affected the uniform flow profile significantly. The stone piers and arches comprising the bridge date to the original construction of the Anio Novus^{49,55}. The three arches of the bridge portion from which the Empiglione Bridge samples were collected, have been attributed to repairs conducted under the Roman emperor Hadrian^{49,55}.

At Roma Vecchia, the Anio Novus aqueduct emerges from the ground and was built directly upon the Aqua Claudia aqueduct, which was itself supported by an arcade up to 10 m in height (Fig. 2A, B)^{21,24}. Three age-equivalent upstream-to-downstream samples of travertine at Roma Vecchia were collected from the floor of a 140 m-long continuous section of the Anio Novus aqueduct¹². These included an upstream 0 m location (sample number RNRV3-2A), an intermediate 9 m location (sample number RNRV3-3A) and a downstream 140 m location (sample number RNRV1-2A; Fig. 1B).

Aqueduct travertine field sample collection. Travertine samples collected from all sites at Galleria Egidio, Empiglione Bridge and Roma Vecchia (Figs. 1, 2) were systematically photographed, measured, and described before careful removal using a hammer and small, clean, well-sharpened chisels composed of hardened steel. Each travertine sample was labelled (e.g., sample number, upstream–downstream context and flow direction determined by contextual orientation the sample within the aqueduct channel), bagged, and shipped in a padded container to the Microscopy and Imaging Core Facility of the Carl R. Woese Institute for Genomic Biology (IGB) at the University of Illinois Urbana-Champaign (Illinois). Samples were cut on a clean water-cooled diamond embedded tile saw in an orientation parallel to the upstream–downstream flow direction of the channel. Samples were then thoroughly washed with deionized water, polished, dried in a clean room, and photographed with a Nikon SLR D7000 digital camera (Nikon, Japan).

Petrographic thin-section preparation and optical microscopy. Billets cut from the three travertine samples collected at Roma Vecchia (Fig. 1B) were prepared by Wagner Petrographic (Linden, Utah) as Petro epoxy impregnated, doubly polished, uncovered, 25 µm-thick sections mounted on standard-sized petrographic glass slides. Optical microscopy of these thin sections was completed on a Hamamatsu Nanozoomer digital slide scanner using a 20×0.75 NA UPlansApo objective at a pixel resolution of 0.23 µm under a brightfield (transmitted light) modality. Further detailed descriptions of the light, laser, electron, and x-ray microscopy techniques used to analyze the Anio Novus aqueduct travertine samples are presented in Sivaguru et al. (2022).

Hydraulic measurements. Each of the Anio Novus travertine crystal growth ripple morphology samples analyzed in the present study were carefully photographed, measured and marked to record their precise position, three-dimensional (3D) distribution, and upstream to downstream orientation within the aqueduct channel. This included measurement of the wetted perimeter and cross-sectional flow area of the aqueduct channel at each site²³, techniques presented in²⁴. Reconstruction of the flow rate of the ancient Anio Novus aqueduct water was done by assuming uniform flow, which is justified and accurate if: (1) the channel cross-section, gradient and direction are roughly constant; and (2) the sample site is away from hydraulic control points, such as sluice gates, junctions, or branches. Many of ancient Rome's aqueduct channels cannot be studied because they have been destroyed, or are inaccessible due their height above ground, depth underground, or because the channel is filled with sediment and soil. Although these factors make the widespread regional mapping and analysis of aqueduct travertine ripples challenging, three sites were identified within the Anio Novus aqueduct (Fig. 1) that meet these criteria and exhibit mm- to cm-scale travertine crystal growth ripples (Figs. 3 and 4).

The slope of the Anio Novus aqueduct channel floor at Roma Vecchia was calculated using previously reported topographic elevation⁵⁴, while distances between each elevation point were calculated using ArcGIS^{23,24}. In addition, previously determined channel and travertine geometry data were used for both Galleria Egidio and Roma Vecchia^{23,24}. The channel at Empiglione Bridge could not be accessed due to its height above ground level. A Leica total station (Leica Camera AG, Wetzlar, Germany) was used to measure the geometry of the channel and the travertine crystal growth ripple morphologies (Supplementary Fig. S5) and then processed in the SolidWorks 2015 Premium × 64 SP5.0 program (Dassault Systèmes SE, Vélizy-Villacoublay, France).

Characterization of travertine crystal growth ripples. Variations in the morphological characteristics of the Anio Novus travertine crystal growth ripples through time (i.e., along vertical stratigraphic cross-sections at each geographic location) and space (i.e., at different sample locations along the channel flow path) were qualitatively and quantitatively investigated. Bottom-to-top analyses of the travertine crystal growth ripple layers through the entirety of the 8 cm-thick stratigraphy, which records changes through time at three locations at Roma Vecchia, was evaluated using digital image analysis of individual stratigraphic horizons (described below). These were further evaluated with direct hand-sample and thin-section images analyses and measurement using open-source NIH ImageJ software. A total of 21 specific travertine crystal growth ripple layers (stratigraphic horizons), each representing the travertine-water growth interface at any given specific point in time, were evaluated. These were consistently identified within digital scans of Roma Vecchia hand-sample cross-sections by tracking individual dark laminae. The shape of each layer of travertine crystal growth ripples was then determined using the Livewire function in the MIPAV program (National Institutes of Health, USA, <https://mipav.cit.nih.gov/>). Finally, each horizon was analysed in MATLAB (MathWorks, Natick, MA, USA) with the results collated and compared with direct sample measurement performed in MIPAV, Adobe Photoshop and Microsoft Excel (Microsoft, Redmond, WA, USA).

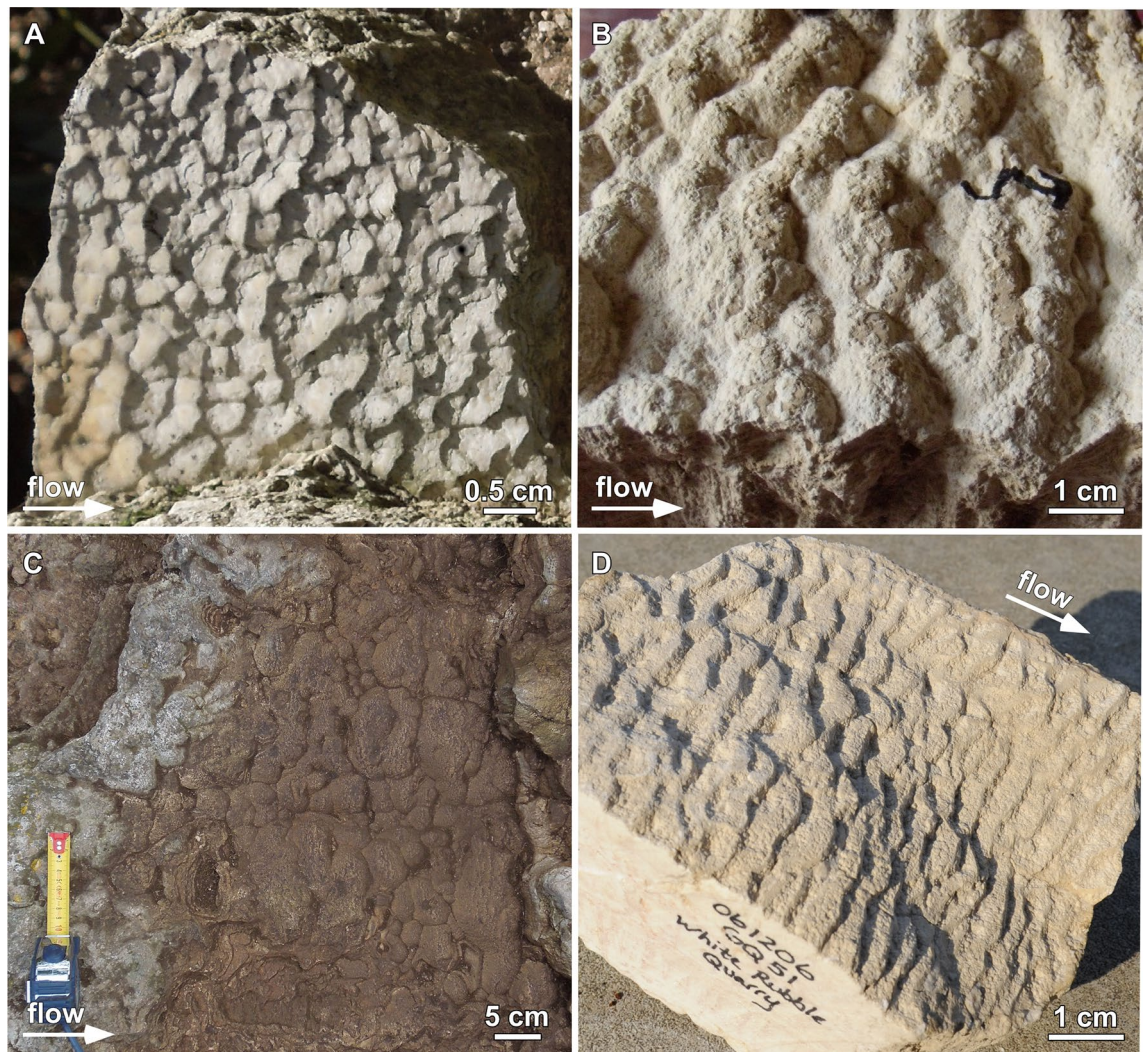
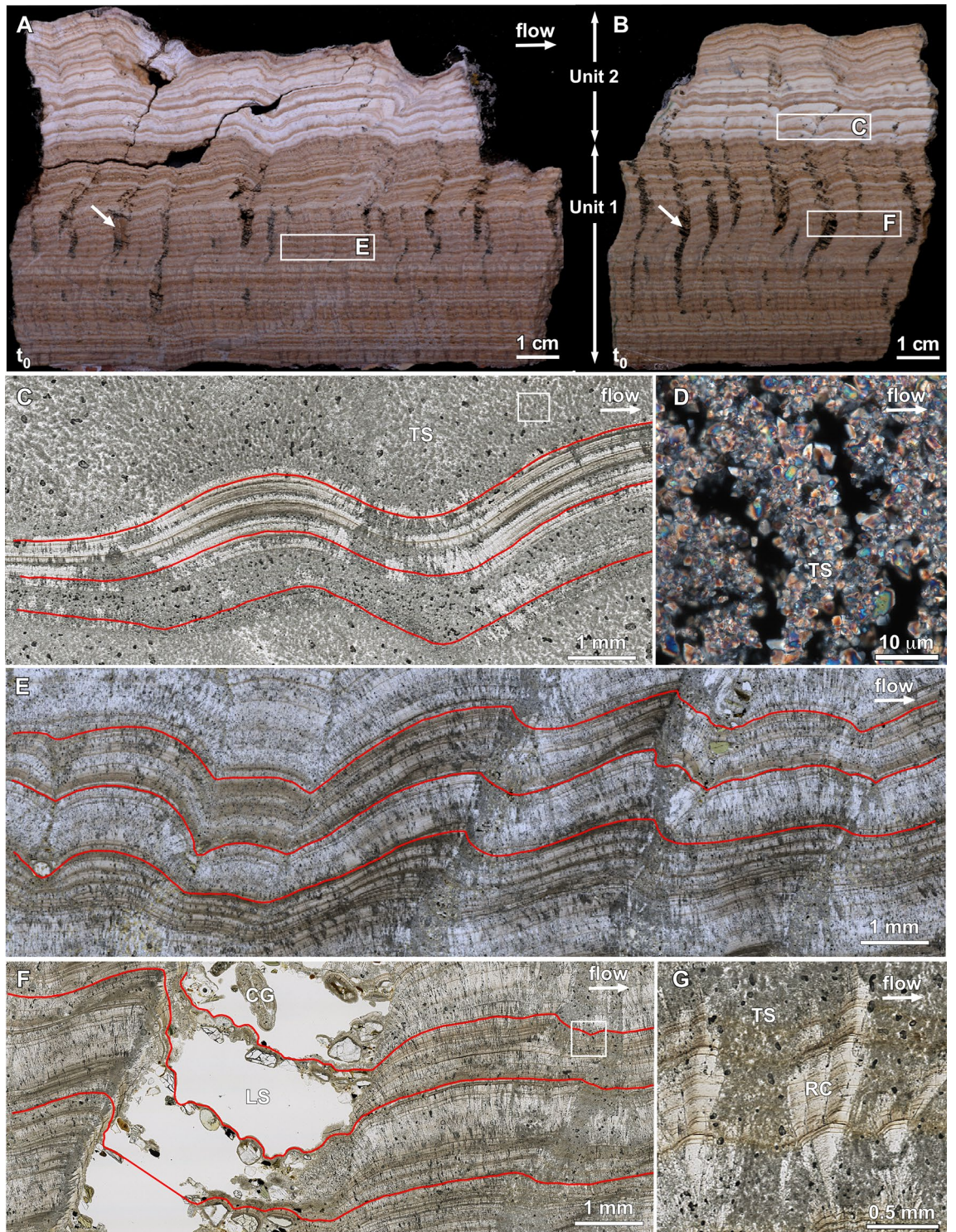


Figure 3. Comparison of different types of travertine crystal growth ripple morphologies deposited in the Anio Novus aqueduct with travertine microterraccette morphologies deposited in hot-spring drainage systems. (A–C) Anio Novus travertine crystal growth ripple morphologies formed at the three Roma Vecchia sample sites (Fig. 1B). (A) Linguoid travertine crystal growth ripples at RF 0 m; (B) sinuous ripples at RF 9 m. (C) Hummocky travertine crystal growth ripples at RF 140 m. (D) Pleistocene-age Distal-Slope Facies travertine microterraccette morphologies deposited in the quarries of Gardiner, Montana (modified from²).

Three primary geometric characteristics of the travertine crystal growth ripples were analysed including wavelength (λ), amplitude ($a = 0.5 \times$ ripple height [Δ]), and steepness ($= \Delta/\lambda$). Ripple wavelengths were analysed by Fourier transform. The Lomb-Scargle algorithm was implemented with Welch-Overlapped Segment Averaging (WOSA, 50% overlapping periodograms) to produce Fourier transforms of each stratigraphic horizon. Peak identifications from the resulting power spectrum were tested for significance against either: (1) a white-noise (random) null hypothesis; or (2) an autoregressive red-noise null hypothesis where each point depends on the point before it. The red noise character is defined as decreasing spectral power with increasing wavenumber. Confidence limits ($= 1 - (1/n)$, where n is the number of points sampled by Mipav along the ripples)⁵⁶ were calculated using 1000 Monte Carlo simulations.

Four different proxies (described in Supplementary Information S5.3) for amplitude were then calculated from the ripple horizons for RF 140 m (Fig. 1B). Ground truthing (measurement of amplitude of ripples in NIH software ImageJ) showed that the most accurate proxy was the mean of the displacement of the background-subtracted horizon (Supplementary Fig. S6) and this proxy was also calculated for the other samples.

The aim of investigating variations in travertine crystal growth ripples at the three sites along the Anio Novus aqueduct channel flow path (Fig. 1B) was to evaluate the relation between the flow properties and the ripple wavelength in the flow direction. A single stratigraphic horizon composed of travertine crystal growth ripples was investigated at each of the three sites. These were: (1) the “latest flow” at Empiglione Bridge (the rippled surface visible in Fig. 2C); (2) the “early flow” at Galleria Egidio; and (3) the “latest flow” at Roma Vecchia. The “latest flow” at Roma Vecchia is 19 cm above (and hence deposited later than) the top of the Unit 2 (Fig. 4), and located 1 m upstream (Fig. 3D). At each stratigraphic position, representative depositional surfaces and a



◀**Figure 4.** Dark–light laminae stratigraphy of travertine hand-sample cross-sections deposited within the Anio Novus aqueduct. Samples were collected from the upstream RF 0 m (Sample Number: RNRV3-2A; **A**) and downstream RF 140 m (Sample Number: RNRV1-2A; **B**) sites at Roma Vecchia (Fig. 1B). Travertine depositional Units 1 and 2 and downstream flow direction (white arrows) are indicated. Modified from¹². (**A**) and (**B**). Standard reflected light hand-sample photographs of the face of vertical cross-sections oriented parallel to the downstream flow direction. Depositional age was determined via correlation of the t_0 contact surface between the underlying mortar and overlying travertine. Lee sands were deposited on the lee side of each travertine crystal growth ripple morphology (white arrows in **A** and **B**). (**C**) Nanozoomer brightfield (transmitted plane light) thin-section photomicrograph (white box C in **B**) showing travertine shrubs (TS). Tracings of three representative linguoid travertine crystal growth ripple morphology cross-sections are shown (red lines). (**D**) Polarized light high-resolution widefield photomicrograph (enlargement of white box in **C**) of dendritically branching aggregates (shrubs) of 1 to 3 μm -diameter euhedral calcite crystals. (**E**) Nanozoomer brightfield thin-section photomicrograph (Box E in **A**). Tracings of three representative linguoid travertine crystal growth ripple morphology cross-sections are shown (red lines). (**F**) Nanozoomer brightfield thin-section photomicrograph (white box in **F**). Tracings of three representative linguoid travertine crystal growth ripple morphology cross-sections are shown (red lines). Labels indicate regions of lee sands (LS) with coated grains (CG) that were partially removed during cutting and thin-section preparation. (**G**) Enlargement of white box in (**F**). Diagenetic replacement radiaxial calcite (RC) crystals form upward radiating bundles that crosscut the original travertine shrubs (TS) and alternating dark–light laminae stratigraphy.

two-dimensional (2D) vertical cross-section of the travertine samples, each from different locations on the wetted perimeter, was analysed to estimate a boundary-averaged wavelength. More than 30 wavelength measurements for each site were made and the Sauter mean wavelength ($\bar{\lambda}_{32}$) estimated, following accepted practice⁵⁸.

Travertine samples chosen for analysis were deposited directly onto the uppermost surface of the mortar lining of the Anio Novus aqueduct channel and exhibited complete and continuous stratigraphic sequences (i.e., no evidence of significant disruption, erosion, or dissolution during deposition). At Empiglione Bridge, measurements of ripple wavelengths of the travertine surface were made at the vault (1.9 m above the floor) and two locations (at 1.3 m and 0.9 m above the floor) on the left-hand wall (when facing downstream, Fig. 2C), using the Leica total station as described above. At Galleria Egidio (Supplementary Fig. S7) and Roma Vecchia (Supplementary Fig. S8), ripple wavelengths in the centre of the channel floor were measured from photographs taken perpendicular to the travertine surface. Wavelengths and ripple height were measured on scans of polished cross-sections of travertine crystal growth ripple stratigraphy from the “latest flow” at Empiglione Bridge (where samples were collected immediately downstream of the measured section, Supplementary Fig. S9), from the wall of the “early flow” at Galleria Egidio (Supplementary Fig. S10) and the floor of the “latest flow” at Roma Vecchia (Supplementary Fig. S11). These samples were all less than 3 wavelengths in length in the downstream direction, therefore ripples were measured directly in ImageJ rather than by Fourier transform.

Results

Travertine stratigraphy and crystal growth ripple morphology. Detailed analyses of the crystalline structure, sedimentology, stratigraphy, and diagenetic alteration of the three travertine samples within the Anio Novus aqueduct channel at Roma Vecchia (Fig. 1B) are presented in Sivaguru et al.¹². The following summary provides a fundamentally important depositional and diagenetic context for characterization of the Anio Novus travertine crystal growth ripple morphology in the present study. The Anio Novus aqueduct travertine deposited at each of the three Roma Vecchia sites (Fig. 1B) is composed of: (1) the top of the underlying Roman mortar on the floor of the aqueduct; (2) the time-zero (t_0) surface comprising the contact between the underlying mortar and the overlying travertine; and (3) an 8 cm-thick deposit of aqueduct travertine composed of an underlying 5 cm-thick Unit 1 and an overlying 3 cm-thick Unit 2¹². Travertine crystal growth ripples observed in three-dimensions (3D) on in situ bedding surfaces and hand samples (Fig. 3), as well as throughout all vertical slices of collected samples (Fig. 4), are described in the following. Age-equivalency of the three Roma Vecchia travertine samples (Fig. 1B) was established via correlation of the t_0 surface, their compositional and stratigraphic consistency in crystalline texture, color, thickness and layering, and the lack of evidence for any later alteration, disturbance, or dissolution during possible Roman maintenance (Fig. 4)¹².

The Unit 1 and 2 travertine deposits (Fig. 4A, B) are composed of two types of calcium carbonate (CaCO_3) morphologies, which include: (1) original 50 to 100 μm -tall dendritically branching aggregates of small (1–3 μm -diameter) euhedral calcite crystals (Fig. 4C; called *shrubs*); and (2) variably sized (100's μm to 10's mm) diagenetic replacement *radiaxial calcite* crystals that form upward radiating bundles that crosscut the alternating dark–light laminae stratigraphy but do not influence the original travertine crystal growth ripple morphologies (Fig. 4D, E)¹². Both types contain stratigraphic sequences of interlayered dark brown and light beige laminae (< 10 to 100 μm -thick), formed by organic matter entrapped during original crystallization and deposition (Fig. 4)¹². Unit 1 travertine is composed of high-frequency interlayering of 0.1 to 1 mm-thick dark brown laminae and light beige laminae that are generally planar, yet sometimes exhibit low angle angular unconformities (Fig. 4A, B). While the thickness of the dark brown laminae remains relatively consistent in Unit 1 and 2 (100's μm -thick to ~ 1 mm-thick), the light beige laminae are significantly thicker in Unit 2 (~ 1–3 mm-thick; Fig. 4A, B).

Unit 1 exhibits travertine crystal growth ripples with stoss, crest, lee and trough geomorphologies (Figs. 4 and 5; Supplementary Videos S1 and S2)^{12,28,30,31}. On bedding surfaces observed in the field, in hand sample and in thin section (Figs. 3, 4, and 5B, C), these travertine crystal growth ripples exhibit wavelengths generally increasing from mm scale near the bottom to cm scale near the top and are morphologically consistent with linguoid,

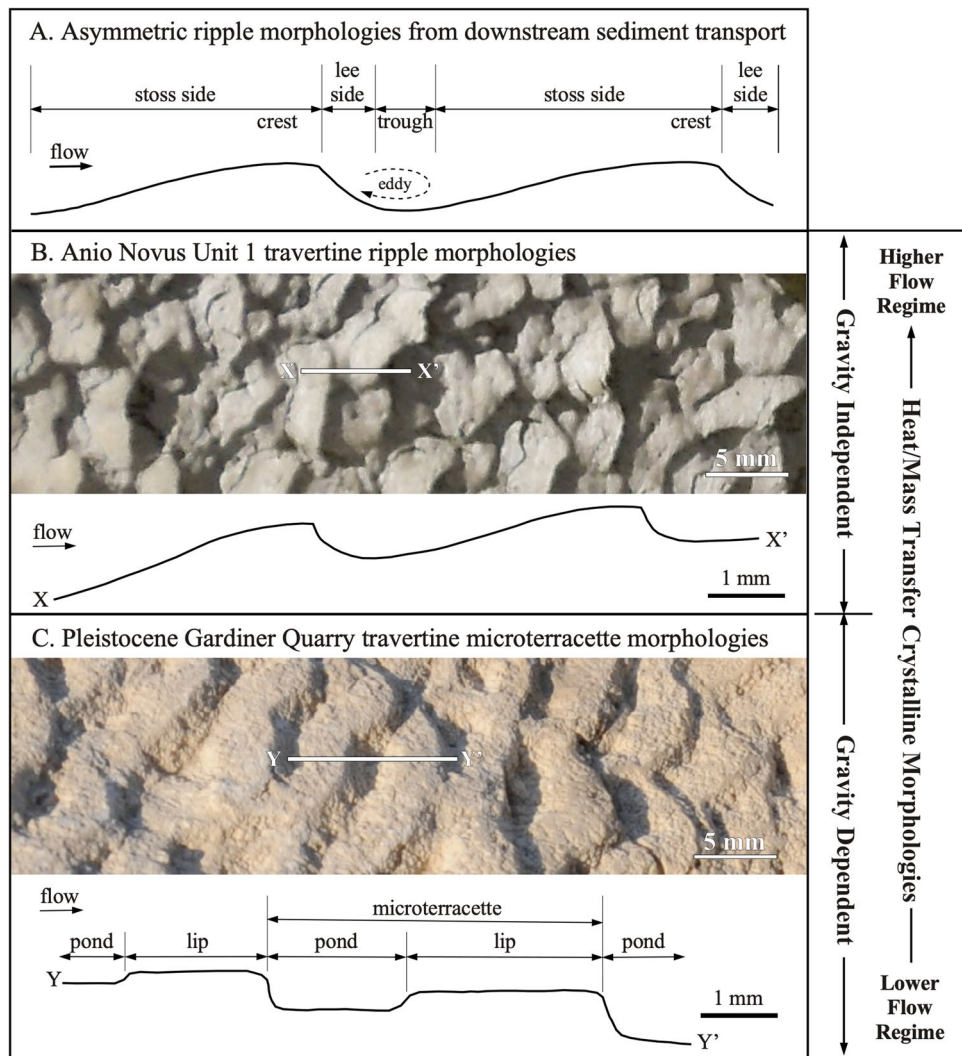


Figure 5. Comparison between Anio Novus travertine crystal growth ripple morphologies and Gardiner Quarry travertine microterraccette morphologies. (A) Terminology used to describe the geomorphology of asymmetric ripples formed by downstream hydraulic transport of sedimentary grains^{28,30,31}. (B) Enlargement of Anio Novus Unit 1 travertine linguoid travertine crystal growth ripple morphologies shown in Fig. 3A. X–X' is the line of section shown for the morphology cross-section tracing shown in Fig. 4E. (C) Enlargement of Pleistocene Gardiner Quarry Distal-Slope Facies travertine microterraccette morphology shown in Fig. 3D. Y–Y' is the line of section shown in the morphology cross-section tracing.

sinuous and hummocky ripples observed in sedimentary transport ripples^{12,28,30,31}. As these layers of travertine crystal growth ripples accumulated vertically, the position of the crests and troughs intermittently preferentially accumulated in a downstream direction (*prograded*) and at other times in an upstream direction (*retrograded*), forming zig-zag stratigraphic patterns in 2D vertical sections (Figs. 3 and 4)¹² (Supplementary Videos S1 and S2, described in more detail in Supplementary Information S3.1). In Unit 2, the travertine crystal growth ripple wavelengths are generally on the cm scale and larger than those in Unit 1, forming sinuous and hummocky sedimentary transport ripples (Figs. 4 and 5)^{12,28,30,31}. As in Unit 1, the ripple sets in Unit 2 prograde and retrograde up-section, which again form zig-zag stratigraphic patterns in 2D vertical sections (Figs. 3, 4; Supplementary Videos S1 and S2). A common feature of the Unit 1 and 2 travertine, which further accentuates the travertine crystal growth ripple morphology, is the deposition of siliciclastic sand grains within eddies on the lee slope of ripple sets (Figs. 4A, B, D, 5A), called *lee sands*¹² (Fig. 3A–C). These lag deposits contain a minor component of an assortment of fine- to coarse-grained and angular to rounded siliciclastic sands¹². MicroCT imaging prior to hand-sample cutting indicates that these sands were originally densely packed on the lee side of each ripple prior to being washed out and plucked during sample preparation, leaving behind void spaces (Fig. 4A, B)¹².

Quantitative characterization of travertine crystal-growth ripples. Our approach to quantifying up-section stratigraphic variation in travertine crystal growth ripple geomorphology for the 0, 9 and 140 m samples collected at Roma Vecchia (Fig. 1B) are shown in Fig. 6. The digital horizons analysed by Fourier transform

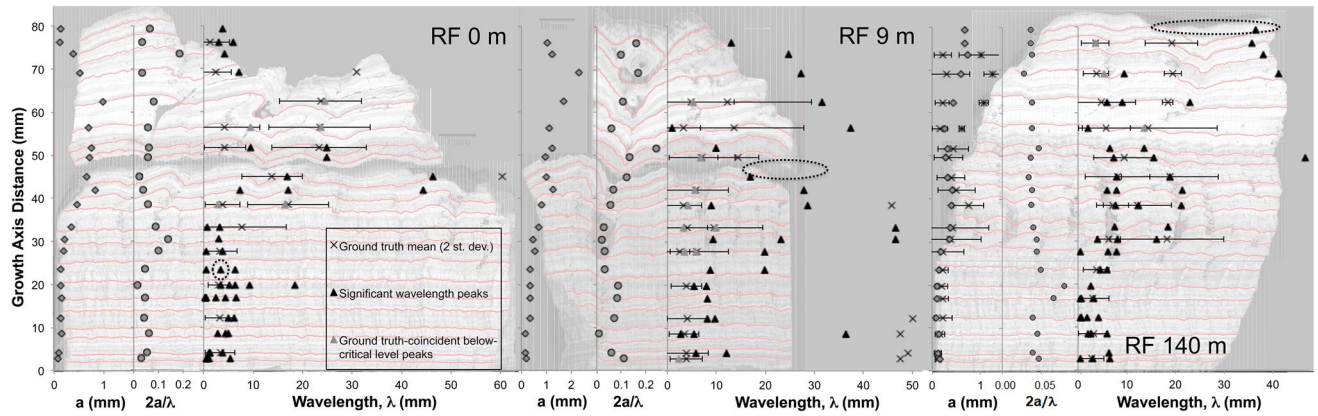


Figure 6. Travertine crystal growth ripple morphology cross-section measurements and characterization within stratigraphic cross sections of the Anio Novus aqueduct deposits at Roma Vecchia (Fig. 1B). The thickness of vertical travertine accumulation from the time-zero surface (t_0) is plotted on the y-axis. Aqueduct water flow direction is from left to right in all three images. Travertine wavelength (λ) is shown on the x-axis, as well as uncertainty bars corresponding to two standard deviations. Left: Sample RF 0 m (number of samples analysed (n) = 21). Center: Sample RF 9 m (n = 20). Right: RF 140 m (n = 21). Data is presented in Supplementary Data Files 1–3.

are shown by red line tracings overlaid on the hand-sample images (Fig. 6). There is generally good agreement between the shortest significant wavelengths identified by the Fourier transform (shown as black triangles) and ground-truthed wavelengths (shown by crosses). After initial establishment of the travertine crystal growth ripples at the base of Unit 1 (Fig. 4A, B), a cyclic stratigraphic succession of ripple wavelength and amplitude occurs from increasing, to decreasing and increasing again.

The calculation of Re_c^* from mean travertine crystal growth ripple morphology wavelength, water temperature and kinematic viscosity and shear velocity has been completed at the three different sites along the flow path of the Anio Novus (Fig. 1A). Full measurements of travertine crystal growth ripple characteristics and results are provided in the Supplementary Information (S3.2).

Calculation of critical shear Reynolds number from aqueduct travertine crystal-growth ripples. Shear velocity, u^* , and Re_c^* (Supplementary Table S2) were computed using Eqs. (1) and (3), respectively. In fluid-sediment systems, the boundary-averaged shear velocity (u^*) is a means of expressing the boundary-averaged shear stress in units of velocity. u^* can be determined from estimates of aqueduct longitudinal slope (S) and hydraulic radius (R_h) by assuming uniform flow conditions, where⁵⁹:

$$u^* = \sqrt{\frac{\tau_b}{\rho}} = \sqrt{gR_h S} \quad (1)$$

where τ_b is the boundary-averaged shear stress, ρ is the mass density of water, g is the acceleration of gravity, and S is the aqueduct floor slope (gradient). Equation (1) for shear velocity u^* is based on the assumption of uniform flow and accounts, through the use of the hydraulic radius, for the irregular (associated with travertine deposition) and taller-than-wide shape of the wetted boundaries. Furthermore, it provides a value averaged over the whole wetted boundary. The present study has therefore adopted the assumption of uniform flow and based hydraulic computations on the geometric property of aqueduct channel hydraulic radius, defined as the ratio of flow area to wetted perimeter. The hydraulic radius R_h is given by

$$R_h = \frac{A}{P} \quad (2)$$

where A is the flow area and P is the wetted perimeter, which were estimated based on the travertine deposits on the floor and side walls of the cross section (e.g. Supplementary Fig. S12).

Investigations on a wide variety of mature convective heat/mass transfer crystalline morphologies have consistently found that ripple wavelength scales with the ratio between the water kinematic viscosity and the shear velocity (i.e., the thickness of the viscous sublayer). Furthermore, the shear-velocity based (or friction-based) Reynolds number Re^* has a constant critical value for the formation of different types of mass transfer morphologies^{41,60–62}. This critical shear velocity-based Reynolds number Re_c^* is calculated as:

$$Re_c^* = \frac{u^* \bar{\lambda}}{\nu} \quad (3)$$

where $\bar{\lambda}$ is the boundary-averaged ripple wavelength and ν is the kinematic viscosity of water, which is a function of water temperature. Curl⁵⁷ derived the following relationship between u^* , the mean (cross-sectionally-averaged) flow velocity (\bar{u}) and the Sauter mean of the measured ripple wavelengths ($\bar{\lambda}_{32}$) for dissolution morphologies formed in a circular conduit:

$$\bar{u} = u^* \left(2.5 \left[\ln \left\{ \frac{D}{2\lambda_{32}} \right\} - \frac{3}{2} \right] + B_L \right) \quad (4)$$

where D is the diameter of the conduit and B_L is Prandtl's bed-roughness constant. B_L is a constant for dissolution morphologies of a particular shape and Re_c^* , once they have reached equilibrium with an imposed mean velocity \bar{u} ^{57,60}.

Derivation of morphology roughness-flow relationships. We have modified Eq. (4) for use in the taller-than-wide, rectangular aqueduct channel through inclusion of the hydraulic radius (defined in Eq. 2), knowing that, for a circular conduit, $R_h = D/4$:

$$\bar{u} = u^* \left(2.5 \left[\ln \left\{ \frac{2R_h}{\lambda_{32}} \right\} - \frac{3}{2} \right] + B_L \right) \quad (5)$$

Substituting u^* from Eq. (1) into Eq. (5) gives,

$$\bar{u} = \sqrt{gR_h S} \left(2.5 \left[\ln \left\{ \frac{2R_h}{\lambda_{32}} \right\} - \frac{3}{2} \right] + B_L \right) \quad (6)$$

Temperature determines the density and kinematic viscosity of water flows⁶³, which in turn affects the flow depth and R_h . Through its incorporation of R_h , Eq. (6) thus negates the need to estimate the temperature of the flow that formed the travertine crystal growth ripples to estimate \bar{u} . If the wetted perimeter P and flow area A can be measured or estimated from the surviving travertine stratigraphy, then R_h can be estimated from Eq. (2) and substituted into Eq. (6) to calculate \bar{u} . Then an estimation of flow rate, Q , can be made using the following continuity equation:

$$Q = A\bar{u} \quad (7)$$

Discussion

Travertine crystal growth ripples. The stoss, crest, lee, and trough geomorphology of the Anio Novus travertine crystal growth ripples are consistently observed in 3D bedding surfaces (Figs. 2C, 3A–C, 5B, C) and in vertical 2D sections of hand samples and in 2D thin section (Fig. 4). While the complex physical, chemical, and biological processes controlling the travertine crystal growth ripples are distinctly different from those controlling sediment transport ripples^{28,32} and solution ripples⁴², the basic ripple nomenclature established in these previous studies provides an important comparative context for describing the travertine crystal growth ripple morphologies^{28,30,31} (Figs. 3A–C, 4, 5). Of particular importance is that, in addition to their formation on the channel floor, the travertine crystal growth ripple morphologies of the Anio Novus also formed horizontally on the vertical surfaces of the aqueduct channel walls, such as those observed at Empiglione Bridge (Fig. 2C). This evidence indicates that the Anio Novus travertine crystal growth ripple morphologies are independent of gravitational forces (Fig. 5B, C). Similarly, non-gravity dependent flute, scallop, and ripple morphologies have been observed to form on the vertical walls and ceilings of ice and dissolving cave systems^{34,35,37,38,42}. Conversely, all ripples formed from the downstream transport of suspended sediments are gravity dependent^{28–31,40}, drawing another fundamental distinction with the Anio Novus aqueduct travertine crystal growth ripples.

Another previously well-studied class of gravity dependent heat/mass transport morphologies in travertine, called *microterraces*, form in many different earth surface (i.e., lakes, rivers, cold- and hot-springs) and subsurface (e.g., caves, fractures) environments^{2,3,42}. Each microterrace is structurally composed of a terraced pond and a lip, which create a gravity-driven cascading downstream sequence^{2,3,64} (Fig. 4D). Travertine microterrace morphologies are therefore geomorphologically distinct from the Anio Novus travertine crystal growth ripples (Fig. 5A–D) and are representative of deposition in fundamentally different gravity-independent regimes with respect to overall hydraulics, geochemistry, and biological activity^{2,28,43,44,65,66}.

Valuable insights are provided via direct comparison of the Anio Novus travertine crystal growth ripple morphology with both modern and ancient Distal-Slope Facies travertine microterraces deposited at Mammoth Hot Springs in Yellowstone National Park and in nearby Gardiner, Montana^{2,64,67,68}. The Anio Novus travertine crystal growth ripples, which are slightly younger than the 38–52 CE age of the aqueduct itself¹², were precipitated from the following gravity-independent aqueous conditions: (1) temperature = 6°–13.5 °C, pH = 7.8–8.4, and saturated with respect to carbonate mineral precipitation^{53,69,70}; and (2) water depth = 1–2 m, flow velocity = 0.8–1.8 m/s, and highly turbulent confined channel flow^{12,23,24} (Fig. 5, Supplementary Table S3, Supplementary Figures S5, S13). In contrast, the Mammoth-Gardiner Distal-Slope Facies travertine microterraces, which are modern to recent (0–8000 years old) at Mammoth and Pleistocene (19,500–38,700 years old) in the Gardiner quarries², were precipitated under the following gravity-dependent, unconfined, nearly laminar sheet-flow aqueous conditions: (1) temperature = 28–44 °C; (2) pH = 7.3–8.1; (3) supersaturation (Ω) = 2–5; (4) water depth = 1–3 cm; and (6) flow velocity = < 0.01–0.1 m/s^{2,44,64,68,71}.

These comparisons reveal that the aqueous temperatures and chemistries are comparable between the formation of the Anio Novus travertine crystal growth ripples and the Mammoth-Gardiner travertine microterraces, respectively. Furthermore, the mineralogy and crystalline structure of travertine crystal growth ripples and microterraces are generally comparable. The Anio Novus travertine crystal growth ripples are composed of small 1–3 μm -diameter euhedral calcite crystals that form larger 100–500 μm -tall shrub-like aggregates¹² (Fig. 4C, D). The Distal-Slope Facies microterraces are composed of 1–3 μm -diameter euhedral calcite crystals

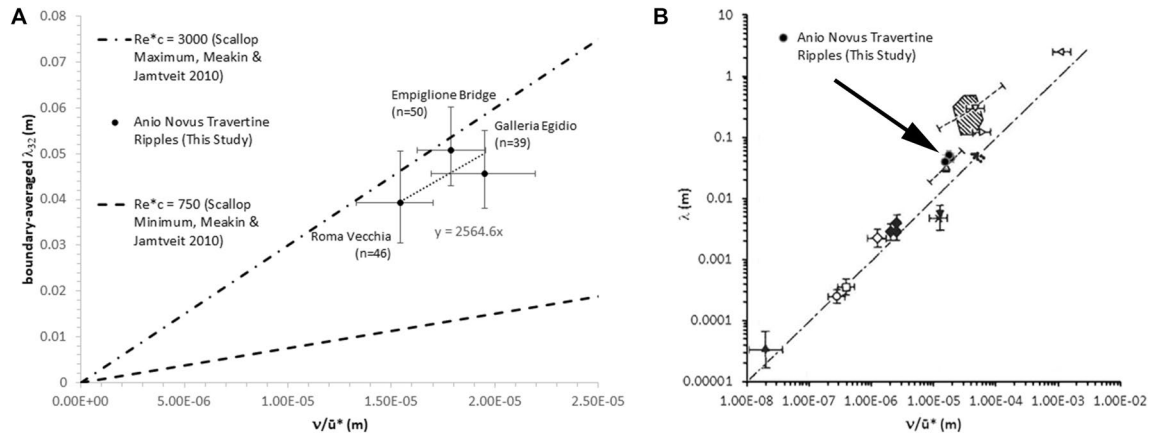


Figure 7. Covariation between u^* and $\bar{\lambda}_{32}$ (see Supplementary Table S2). (A) Data from this study falling within dashed lines representing Meakin and Jamtveit (2010)'s range for Re^* of scallop formation. “n” refers to number of measurements from which $\bar{\lambda}_{32}$ was calculated. Dotted line is a linear regression with details shown on the chart. Uncertainty bars correspond to two standard deviations. (B) The same Anio Novus travertine crystal growth ripple data (from A) now plotted over Thomas⁶¹ log–log plot of data from sediment transport ripples, solution ripples (scallops eroded on metal, limestone, bitumen and plaster surfaces) and ice ripples. Anio Novus travertine data plot amongst these other ripple and scallop data (used with permission).

that form 100 μm -tall shrub-like crystalline aggregates^{2,64,68}. However, in stark contrast, there are orders-of-magnitude differences in the contextual flow regimes from which the Anio Novus travertine crystal growth ripples and Mammoth-Gardiner microterraces were deposited, respectively.

Hydraulic reconstructions from travertine crystal growth ripples. As described in the previous section, the travertine crystal growth ripples formed within the channel of the Anio Novus aqueduct are generally similar in 2D vertical section morphology to well-studied ripples formed during the downstream hydraulic transport of sedimentary grains (Fig. 5)²⁸. This is despite having been formed under very different physical, chemical, and biological environmental conditions^{2,3,28,31}, which is reflected in the morphology observed on 3D surfaces (Fig. 5). Importantly, Hanratty³³ formulated a fluid mechanical theoretical framework for the development of instabilities on surfaces that are eroding, dissolving, or being precipitated. Results indicate that wave-induced turbulent flow is equally influential during convective diffusion controlling travertine CaCO_3 crystal precipitation, as well as downstream sediment transport. Therefore, the hydraulic history of open-channel turbulent flow can be equally reliably reconstructed from both travertine crystal growth ripples and sediment transport ripple morphologies³³.

To compare aqueduct travertine crystal growth ripples characteristics with those of other heat/mass transfer crystalline morphologies (Supplementary Information S4.1), Supplementary Table S1 summarizes estimates of the ripple wavelengths at Empiglione Bridge (“latest flow”), Galleria Egidio (“early flow”), and Roma Vecchia (“latest flow”). Supplementary Table S2 establishes the shear velocity, Reynolds number and other flow properties from the data in Supplementary Table S1. The aim is to evaluate a possible relation between ripple wavelength along the flow direction and other flow properties. This was completed on the travertine crystal growth ripples observed in 2D channel sections from the three sites along the Anio Novus. Requirements included having enough travertine preserved to determine the hydraulic radius (R_h), given by the ratio of flow area A and wetted perimeter P (Eq. 2), could be reconstructed and where the assumption of uniform flow is valid^{23,24}.

Figure 7 plots v/u^* versus $\bar{\lambda}_{32}$ for the three sample sites along the Anio Novus flow path (Fig. 1A), all the sites available due to the limited survival and accessibility of archaeological remains. The wavelength for each of these 3 points is averaged from the wavelengths of 39–50 individual travertine crystal growth ripples at that location (Supplementary Information S5.3, Supplementary Figures S7–S11). Uncertainties and approximations also resulted from data collection challenges related to the evaluation of: (1) channel slope (Galleria Egidio) and wetted perimeter (Roma Vecchia); (2) the shear velocity estimate (carried out using a uniform-flow assumption and a boundary-averaged expression for the shear stress) and (3) the fluid viscosity (computed for constant water temperature, which is a reasonable approximation in the aqueduct based on the water temperature data at the source, Supplementary Information S5.4). Nevertheless, the critical shear Reynolds numbers for travertine crystal growth ripple formation for each site (Supplementary Table S2) and for the Anio Novus overall (c. 2565, obtained by linear regression between the sites, Fig. 7A) consistently fall within the range of previously measured dissolution and precipitation morphologies, such as $750 \lesssim Re_c^* \lesssim 3000$ ^{41,61,72,73}. The linear relationship suggested by the data shown in Fig. 7A. is in close agreement with past work on a large variety of morphologies (such as scallops and ripples, formed both by sediment grain deposition³² and crystalline precipitation/dissolution⁴²), which found a linear relationship between these same properties of v/u^* and λ (Fig. 7B). This suggests that, as in dissolution morphologies^{42,72}, the ripple wavelength scales with the thickness of the viscous sublayer (δ), which is commonly estimated as $11.6 v/u^*$ ³⁹. In other words, if the thickness of the viscous sublayer increases, so does the ripple wavelength. More precise data are clearly needed, and additional sites within the Anio Novus deposits

exhibiting travertine crystal growth ripples will be sought in future studies where uniform flow can be assumed and where slope, wetted perimeter, flow area and ripple wavelength can be measured. Nevertheless, for the first time in aqueduct travertine deposits, this shows that travertine crystal growth ripple wavelength varies due to changes in shear velocity and fluid viscosity (i.e., water temperature⁶³) alone, in accord with Eq. (3).

Unlike dissolution morphologies such as scallops⁴², which dissolve in earlier formed bedrock, travertine crystal growth ripples deposit new layers on top of previous ripple sets, thus recording their history of formation. Therefore, changes in flow conditions and/or temperature over time can be traced upwards through changing travertine crystal growth ripple characteristics (illustrated by the red and green lines in Fig. 4, which provide 2D upward tracing of troughs in vertical section). It is shown above (Fig. 7) that the Anio Novus travertine crystal growth ripples are within the range of critical Re^* for dissolution morphologies, suggesting that Curl's Eq. (4), and hence our Eq. (6), are valid for estimating flow velocity from travertine crystal growth ripple wavelengths. Using Eqs. (6) and (7), flow velocity and rate for the three Anio Novus sites were calculated from travertine crystal growth ripple wavelength and other data in Supplementary Table S2. These results, shown in Supplementary Table S3, illustrate that the mean velocity \bar{u} estimated from travertine crystal growth ripple wavelength is within 12–16% of that obtained using the uniform-flow Manning's equation with an estimated Manning's roughness coefficient (n) typical of a material with similar roughness to the aqueduct travertine. This confirms that Eqs. (4) and (6) are at least broadly valid for interpreting travertine crystal growth ripples. Further confirmation is provided by the travertine crystal growth ripples–flow relationships developed for sediment ripples by Van Rijn⁷⁴ from the resistance equation, which make use of the ripple morphology height, Δ , as well as the ripple wavelength (Supplementary Information, Section S4.3). Moreover, our modified Eq. (6) has the advantage of accounting for changes in travertine crystal growth ripple characteristics over time at a particular site, as well as at different sites along the flow path, permitting the reconstruction of the histories of flow velocities and rates throughout a Roman aqueduct network and in similar networks.

Travertine 2D cross-sections such as those of Units 1 and 2 from the aqueduct floor at Roma Vecchia (Fig. 4A, B) are ideal for such reconstructions, since the up-section changes in ripple wavelength can be traced over time through the stratigraphy. However, the travertine on the walls was too poorly preserved at this location to measure or estimate wetted perimeter, P , and flow area, A , for Units 1 and 2. This meant that hydraulic radius could not be estimated, which precluded the use of Eq. (6). Nevertheless, qualitative changes in flow velocity and rate during Units 1 and 2 can be interpreted. From Eq. (3), increases in travertine crystal growth ripple wavelength only result from decreases in shear velocity and/or increases in kinematic viscosity. Kinematic viscosity will vary with temperature⁶³, but, as detailed in Supplementary Information S4.4, the limited possible range of temperatures means variation in viscosity would have been significantly smaller (+13/–10% of the representative 10 °C value, Supplementary Information S5.4) than the observed variation in wavelength at Roma Vecchia (+/–70–150% of the mean). This means that the majority of observed changes in travertine crystal growth ripple wavelength in depositional Units 1 and 2 of Roma Vecchia travertine were due to changes in shear velocity (i.e., flow discharge) at the site rather than changes in temperature. Whereas changes in shear velocity would have been primarily due to changes in flow velocity rather than other factors (Supplementary Information S4.5). Hence, under near-constant kinematic viscosity, the mean wavelength increases observed in Anio Novus travertine are evidence of decreases in flow velocity and rate in the aqueduct, and vice versa. This is confirmed, theoretically and experimentally, for heat/mass transfer morphologies by many previous studies^{75–80}.

As a result, qualitative changes in flow velocity and rate were reconstructed for the earliest periods of flow that formed the 8-cm basal of the deposit within the Anio Novus aqueduct channel at Roma Vecchia (Fig. 4A, B). This was completed using 2D stratigraphic up-section changes in the wavelength of the travertine crystal growth ripples (Fig. 6) deposited on the previously flat t_0 channel mortar surface or on bed defects. After a period of travertine crystal growth ripple initiation (bottom half of Unit 1), flow rate then decreased markedly (third quarter of Unit 1), as suggested by the increase in ripple wavelength at RF 9 m and 140 m (Figs. 4A, B, 6). Flow rate then increased (top quarter of Unit 1), reducing ripple wavelengths, reaching a maximum at the Unit 1/Unit 2 interface. A second reduction in flow rate occurred in the bottom half of Unit 2, after which flow rate remained relatively constant (according to RF140 m). These reductions likely occurred during the first few centuries of the operation of the Anio Novus, i.e. 52 – c.250 CE, when water demand at Rome was near its peak⁸¹. This interpretation is discussed in more detail in Supplementary Information S4.6.

Implications for reconstructions of climate and human activity. Possible drivers of these changes in flow rate in the Anio Novus include climate variability and human action or inaction. However, neither of these could have pushed the flow rate above the limit of 2 m³/s imposed by the hydraulic constraints and bottlenecks presented above²³. Climate may have affected the flow in Anio Novus by changing the flow rate input at its source, the Aniene River, through changing rainfall amounts in the upstream catchment. This seems unlikely to have been significant, however, since the Aniene River could probably have always supplied more water to the aqueduct than it could carry (Supplementary Information, S4.7). Therefore, human manipulation of aqueduct flow was likely the major control of changes in flow within the Anio Novus rather than climatic variations.

There would have been two predominant forms of human action²¹: (1) intentional removal of water from the aqueduct, either legally sanctioned or fraudulent; and (2) maintenance (or lack thereof). It seems likely that Roman managers would have worked to maintain flow rate in the upstream reaches of the Anio Novus aqueduct as close to the carrying capacity of the channel as possible. Frontinus²¹ regards high flow rates in aqueducts as positive, given the ongoing high demand for water in the city, and laments the loss of water *en route*. Even if there were sluice gates at the aqueduct intake (a contested point^{49,55}) it seems unlikely that these gates were used to reduce inflows significantly below the capacity of the channel. Diversionary channels to lower aqueducts, properties, and towns such as Tivoli, may have exerted some control on flow via the use of sluice gates or other

means^{21,49}. Closing of the sluice gates might also have been used as a means to temporarily impound water within the channel itself⁶². Lack of maintenance²⁰, would have allowed travertine deposition to constrict the channel flow, while its weight may have caused leakage from structural cracks. Such cracks could also have resulted from weathering or earthquakes. Constriction and cracking would both have reduced flow within the aqueduct. Travertine deposits 10 s of cm-thick on the floors, walls and ceiling of the aqueduct channel internal perimeter in many areas of the Anio Novus⁴⁹, at sites such as Osteriola, indicate that regular maintenance was neglected, at least towards the operational demise of the Anio Novus aqueduct.

Conclusions

Travertine crystal growth ripples have been utilized in this study to reconstruct the early hydraulic history of the Anio Novus, the largest and farthest reaching of ancient Rome's 11 aqueducts. Travertine crystallizes from complexly physical, chemical, and biological processes that operate fundamentally differently from those controlling sandstone ripple mark formation. Yet despite these mechanistic distinctions, the hydraulic history of gravity-driven turbulent flow can be reliably reconstructed from travertine crystal growth ripples as they are from sediment transport ripples. As a result, the hydraulic significance of the amplitude and wavelength of travertine crystal growth ripples preserved within aqueduct travertine have been used to reconstruct the hydraulic history of the Anio Novus. This included petrographic characterization and measurement of travertine crystal growth ripples deposited on the channel floor, walls, and roof of the Anio Novus aqueduct, arguably the most significant of the 11 aqueducts that supplied water to Imperial Rome. Of particular importance is that the critical shear Reynolds number of the travertine crystal growth ripples are within the range of hydraulic parameters previously observed to form ripples in multiple other analogous natural and manmade environments. These similarities have been used to further improve upon our previous uniform flow estimates of velocity and discharge for the Anio Novus aqueduct. These relationships establish travertine crystal growth ripple wavelength, defined as the characteristic length of the shear Reynolds number, as a fundamental parameter required to confidently reconstruct maintenance and management of the Anio Novus aqueduct.

Data availability

Raw unprocessed data and images for Main Figures and SI Figures will be made available in the original source format on the University of Illinois cloud data base.

Received: 9 April 2021; Accepted: 7 January 2022

Published online: 24 January 2022

References

- Scarborough, V. L. Water management adaptations in nonindustrial complex societies: An archaeological perspective. *Archaeol. Method Theory* **3**, 101–154 (1991).
- Fouke, B. W. Hot-spring systems geobiology: Abiotic and biotic influences on travertine formation at Mammoth Hot Springs, Yellowstone National Park, USA. *Sedimentology* **58**, 170–219 (2011).
- Pentecost, A. *Travertine* (Springer, 2005).
- Erthal, M. M. *et al.* Shrub morpho-types as indicator for the water flow energy—Tivoli travertine case (Central Italy). *Sediment. Geol.* **347**, 79–99 (2017).
- Janssens, N. *et al.* Fossil travertine system and its palaeofluid provenance, migration and evolution through time: Example from the geothermal area of Acquasanta Terme (Central Italy). *Sediment. Geol.* **398**, 105580 (2020).
- Benjelloun, Y., Carlut, J., Hélie, J.-F., Chazot, G. & Callonnet, L. L. Geochemical study of carbonate concretions from the aqueduct of Nîmes (southern France): A climatic record for the first centuries AD?. *Sci. Rep.* **9**, 5209 (2019).
- Filocamo, E., Carlut, J., Dessales, H., Burckel, P. & Borensztajn, S. Roman builders facing the risk of disaster: Coupling archaeological and geochemical analyses on a section of the 'Aqua Augusta' (the Roman Serino Aqueduct, Southern Italy). *Archaeometry* **60**, 915–932 (2018).
- Hostetter, E., Fouke, B. W. & Lundstrom, C. C. The last flow of water to, and through, the Baths of Caracalla: Age, temperature and chemistry. *J. Anc. Topogr. Riv. Topogr. Antica* **21**, 53–90 (2011).
- Passchier, C. *et al.* The aqueduct of Gerasa—Intra-annual palaeoenvironmental data from Roman Jordan using carbonate deposits. *Palaeogeogr. Palaeoclimatol. Palaeoecol.* **110089** (2020). <https://doi.org/10.1016/j.palaeo.2020.110089>.
- Pons-Branchu, E. *et al.* Three centuries of heavy metal pollution in Paris (France) recorded by urban speleothems. *Sci. Total Environ.* **518**, 86–96 (2015).
- Pons-Branchu, E. *et al.* A geochemical perspective on Parisian urban history based on U-Th dating, laminae counting and yttrium and REE concentrations of recent carbonates in underground aqueducts. *Quat. Geochronol.* **24**, 44–53 (2014).
- Sivaguru, M. *et al.* Depositional and diagenetic history of travertine deposited within the Anio Novus aqueduct of Ancient Rome. In *From the Guajira Desert to the Apennines, and from the Sardinia/Corsica Microplate to the Killer Asteroid: Honoring the Career of Walter Alvarez* (eds. Koebel, C., Claeys, P., and Montanari, S) (Geological Society of America, 2022).
- Sürmelihindi, G., Leveau, P., Spötl, C., Bernard, V. & Passchier, C. W. The second century CE Roman watermills of Barbegal: Unraveling the enigma of one of the oldest industrial complexes. *Sci. Adv.* **4**, eaar3620 (2018).
- Sürmelihindi, G. *et al.* Laminated carbonate deposits in Roman aqueducts: Origin, processes and implications. *Sedimentology* **60**, 961–982 (2013).
- Sürmelihindi, G. & Passchier, C. W. Sinter Analysis. A Tool for the Study of Ancient Aqueducts. In *Historische Wasserleitungen gestern, heute, morgen: Internationales Symposium mit besonderer Berücksichtigung ihrer denkmalgerechten und betriebssicheren Erhaltung*, Wien, 19.-23. Oktober 2011 (ed. Wiplinger, G.) 269–286 (Peeters, 2013).
- Neely, J. A. & Huerta, B. R. C. Una síntesis del manejo prehispánico del agua en el Valle de Tehuacán, Puebla, México. *Arqueología* **182–198** (2014).
- Noel, E. *Qanats*. *J. R. Cent. Asian Soc.* **31**, 191–202 (1944).
- McLaughlan, R. G., Knight, M. J. & Stuetz, R. M. *Fouling and Corrosion of Groundwater Wells. A Research Study* (National Centre for Groundwater Management, University of Technology, Sydney, 1993).
- Keenan-Jones, D. C. *et al.* Hierarchical Stratigraphy of Travertine Deposition in Ancient Roman Aqueducts. in *Lazio e Sabina 10 (Atti del Convegno "Decimo Incontro di Studi sul Lazio e la Sabina", Roma, 4–6 giugno 2013)* (eds. Calandra, E., Ghini, G. & Mari, Z.) 293–5 (Edizioni Quasar, 2014).

20. Dessales, H. Entretien et restauration des aqueducs à Rome, au regard du traité de Frontin. in *Histoire des réseaux d'eau courante dans l'Antiquité : réparations, modifications, réutilisations, abandon, récupération* (Université de Nancy 2, CLSH, 20/11/2009–21/11/2009) (ed. Provost, C. A.-R. et S.) 13–21 (Presses universitaires de Rennes, 2011).
21. Frontinus, S. I. *De aquaeductu urbis Romae*. (Cambridge University Press, 2004).
22. Taylor, R. M. *Public needs and private pleasures : water distribution, the Tiber river and the urban development of ancient Rome*. ('L'Erma' di Bretschneider, 2000).
23. Motta, D., Keenan-Jones, D., Garcia, M. H. & Fouke, B. W. Hydraulic evaluation of the design and operation of Ancient Rome's Anio Novus Aqueduct. *Archaeometry* **59**, 1150–1174 (2017).
24. Keenan-Jones, D. C., Motta, D., Garcia, M. H. & Fouke, B. W. Travertine-based estimates of the amount of water supplied by ancient Rome's Anio Novus aqueduct. *J. Archaeol. Sci. Rep.* **3**, 1–10 (2015).
25. Coleman, S. E., Fedele, J. J. & Garcia, M. H. Closed-conduit bed-form initiation and development. *J. Hydraul. Eng.* **129**, 956–965 (2003).
26. Perillo, M. M. *et al.* A unified model for bedform development and equilibrium under unidirectional, oscillatory and combined-flows. *Sedimentology* **61**, 2063–2085 (2014).
27. Perillo, M. M., Prokocki, E. W., Best, J. L. & García, M. H. Bedform Genesis from Bed Defects under Unidirectional, Oscillatory and Combined Flows. *J. Geophys. Res. Earth Surf.* 2014JF003167 (2014). <https://doi.org/10.1002/2014JF003167>.
28. Garcia, M. H. *Sedimentation Engineering: Processes, Measurements, Modeling, and Practice* (American Society of Civil Engineers, 2008).
29. Devauchelle, O. *et al.* Stability of bedforms in laminar flows with free surface: From bars to ripples. *J. Fluid Mech.* **642**, 329–348 (2010).
30. Boggs, S. *Principles of Sedimentology and Stratigraphy* (Pearson Prentice Hall, 2012).
31. Amos, C. L., Kassem, H. & Friend, P. L. Ripple marks. In *Encyclopedia of Coastal Science* (eds. Finkl, C. W. & Makowski, C.) 1447–1454 (Springer, 2019). <https://doi.org/10.1007/978-3-319-93806-6>.
32. Allen, J.R.L. *Sedimentary Structures: Their Character and Physical Basis*, Volume 2 (Elsevier, 1982).
33. Hanratty, T. J. Stability of surfaces that are dissolving or being formed by convective diffusion. *Annu. Rev. Fluid Mech.* **13**, 231–252 (1981).
34. Camporeale, C., Vesipa, R. & Ridolfi, L. Convective-absolute nature of ripple instabilities on ice and icicles. *Phys. Rev. Fluids* **2**, 053904 (2017).
35. Bushuk, M., Holland, D. M., Stanton, T. P., Stern, A. & Gray, C. Ice scallops: A laboratory investigation of the ice–water interface. *J. Fluid Mech.* **873**, 942–976 (2019).
36. Camporeale, C. & Ridolfi, L. Hydrodynamic-driven stability analysis of morphological patterns on stalactites and implications for cave paleoflow reconstructions. *Phys. Rev. Lett.* **108**, 238501 (2012).
37. Camporeale, C. Hydrodynamically locked morphogenesis in karst and ice flutings. *J. Fluid Mech.* **778**, 89–119 (2015).
38. Yokokawa, M. *et al.* Cyclic steps on ice. *J. Geophys. Res. Earth Surf.* **121**, 1023–1048 (2016).
39. Jamtveit, B. & Hammer, Ø. Sculpting of rocks by reactive fluids. *Geochem. Perspect.* **1**, 341–342 (2012).
40. Camporeale, C. & Ridolfi, L. Ice ripple formation at large Reynolds numbers. *J. Fluid Mech.* **694**, 225–251 (2012).
41. Gale, S. J. The hydraulics of conduit flow in carbonate aquifers. *J. Hydrol.* **70**, 309–327 (1984).
42. Richardson, K. & Carling, P. A. *A Typology of Sculpted Forms in Open Bedrock Channels* (Geological Society of America, 2005). <https://doi.org/10.1130/0-8137-2392-2.1>.
43. Hammer, Ø., Jamtveit, B., Benning, L. G. & Dysthe, D. K. Evolution of fluid chemistry during travertine formation in the Troll thermal springs, Svalbard, Norway. *Geofluids* **5**, 140–150 (2005).
44. Veysey, J. & Goldenfeld, N. Watching rocks grow. *Nat. Phys.* **4**, 310–313 (2008).
45. Dong, Y. *et al.* Physiology, metabolism, and fossilization of hot-spring filamentous microbial mats. *Astrobiology* **19**, 1442–1458 (2019).
46. Della Porta, G., Croci, A., Marini, M. & Kele, S. Depositional architecture, facies character and geochemical signature of the Tivoli travertines (Pleistocene, Acque Albule Basin, Central Italy). *RIPS Riv. Ital. Paleontol. Stratigr.* **123**, 487–540. <https://doi.org/10.13130/2039-4942/9148> (2017).
47. Della Porta, G., Capezzuoli, E. & De Bernardo, A. Facies character and depositional architecture of hydrothermal travertine slope aprons (Pleistocene, Acquasanta Terme, Central Italy). *Mar. Pet. Geol.* **87**, 171–187 (2017).
48. Della Porta, G., Hoppert, M., Hallmann, C., Schneider, D., & Reitner, J. The influence of microbial mats on travertine precipitation in active hydrothermal systems (Central Italy). *The Depositional Record*. 1–45 (2021). <https://doi.org/10.1002/dep2.147>
49. Ashby, T. *The Aqueducts of Ancient Rome*. (Oxford University Press, 1935).
50. Hodge, A. T. *Roman Aqueducts and Water Supply*. (Duckworth, 2002).
51. Morley, N. *Metropolis and hinterland: The city of Rome and the Italian economy, 200 B.C.-A.D. 200*. (Cambridge University Press, 1996).
52. Coates-Stephens, R. The walls and aqueducts of Rome in the Early Middle Ages, AD 500–1000. *J. Roman Stud.* **88**, 239–259 (1998).
53. Bono, P. & Percopo, C. Flow dynamics and erosion rate of a representative karst basin (Upper Aniene River, Central Italy). *Environ. Geol.* **27**, 210–218 (1996).
54. Reina, V., Corbellini, G. & Ducci, G. *Livellazione degli antichi acquedotti romani*. (Tipografia della R. Accademia dei Lincei, 1917).
55. Van Deman, E. B. *The Building of the Roman Aqueducts*. (Carnegie Institution of Washington, 1934).
56. Schulz, M. & Stattegger, K. Spectrum: spectral analysis of unevenly spaced paleoclimatic time series. *Comput. Geosci.* **23**, 929–945 (1997).
57. Curl, R. L. Deducing flow velocity in cave conduits from scallops. *Natl. Speleol. Soc. Bull.* **36**, 1–5 (1974).
58. Springer, G. & Hall, A. Uncertainties associated with the use of erosional cave scallop lengths to calculate stream discharges. *Int. J. Speleol.* **49**, 27–34 (2020).
59. Pope, S. B. *Turbulent Flows*. (Cambridge University Press, 2000).
60. Blumberg, P. N. & Curl, R. L. Experimental and theoretical studies of dissolution roughness. *J. Fluid Mech.* **65**, 735–751 (1974).
61. Thomas, R. M. Size of scallops and ripples formed by flowing water. *Nature* **277**, 281–283 (1979).
62. Thorsness, C. B. & Hanratty, T. J. Stability of dissolving or depositing surfaces. *AIChE J.* **25**, 697–701 (1979).
63. Pátek, J., Hrubý, J., Klomfar, J. & Součková, M. Reference correlations for thermophysical properties of liquid water at 0.1MPa. *J. Phys. Chem. Ref. Data* **38**, 21–29 (2009).
64. Fouke, B. W. *et al.* Depositional facies and aqueous-solid geochemistry of travertine-depositing hot springs (Angel Terrace, Mammoth Hot Springs, Yellowstone National Park, U.S.A.). *J. Sediment. Res.* **70**, 565–585 (2000).
65. Vesipa, R., Camporeale, C. & Ridolfi, L. Thin-film-induced morphological instabilities over calcite surfaces. *Proc. R. Soc. Math. Phys. Eng. Sci.* **471**, 20150031 (2015).
66. Hammer, Ø. *et al.* Calcite precipitation instability under laminar, open-channel flow. *Geochim. Cosmochim. Acta* **72**, 5009–5021 (2008).
67. Fouke, B. W., Bonheyo, G. T., Sanzenbacher, B. & Frias-Lopez, J. Partitioning of bacterial communities between travertine depositional facies at Mammoth Hot Springs, Yellowstone National Park, U.S.A. *Can. J. Earth Sci.* **40**, 1531–1548 (2003).
68. Veysey, J. *et al.* Reconstruction of water temperature, pH, and flux of ancient hot springs from travertine depositional facies. *J. Sediment. Res.* **78**, 69–76 (2008).

69. Bono, P. & Boni, C. Water supply of Rome in antiquity and today. *Environ. Geol.* **27**, 126–134 (1996).
70. Bono, P., Dreybrodt, W., Ercole, S., Percopo, C. & Vosbeck, K. Inorganic calcite precipitation in Tartare karstic spring (Lazio, central Italy): field measurements and theoretical prediction on depositional rates. *Environ. Geol.* **41**, 305–313 (2001).
71. Hammer, Ø., Dysthe, D. K. & Jamtveit, B. Travertine terracing: patterns and mechanisms. *Geol. Soc. Lond. Spec. Publ.* **336**, 345–355 (2010).
72. Claudin, P., Durán, O. & Andreotti, B. Dissolution instability and roughening transition. *J. Fluid Mech.* **832** (2017).
73. Meakin, P. & Jamtveit, B. Geological pattern formation by growth and dissolution in aqueous systems. *Proc. R. Soc. Math. Phys. Eng. Sci.* **466**, 659–694 (2010).
74. van Rijn, L. C. Equivalent roughness of alluvial bed. *J. Hydraul. Div.* **108**, 1215–1218 (1982).
75. Andritsos, N. & Karabelas, A. J. Calcium carbonate scaling in a plate heat exchanger in the presence of particles. *Int. J. Heat Mass Transf.* **46**, 4613–4627 (2003).
76. Andritsos, N. & Karabelas, A. J. The influence of particulates on CaCO₃ scale formation. *J. Heat Transf.* **121**, 225–227 (1999).
77. Curl, R. L. Scallops and flutes. *Trans. Cave Res. Group G. B.* **7**, 121–160 (1966).
78. Goodchild, M. F. & Ford, D. C. Analysis of scallop patterns by simulation under controlled conditions. *J. Geol.* **79**, 52–62 (1971).
79. Murphy, P. J. Scallops. In *Encyclopedia of Caves (Second Edition)* (ed. Culver, W. B. W. C.) 679–683 (Academic Press, 2012).
80. Villien, B., Zheng, Y. & Lister, D. Surface dissolution and the development of scallops. *Chem. Eng. Commun.* **192**, 125–136 (2005).
81. Delile, H. *et al.* Rome's urban story inferred from lead-contaminated waters trapped in its ancient harbor basins. *Proc. Natl. Acad. Sci. U. S. A.* **114**, 10059–10064 (2017).
82. Chanson, H. P. Y. Certains aspects de la conception hydrauliques des aqueducs Romains. *Houille Blanche* **6**, 43–57 (2002).

Acknowledgements

We gratefully acknowledge permission and assistance in conducting this research provided by the Soprintendenza Archeologia, Belle Arti e Paesaggio per l'Area Metropolitana di Roma, la Provincia di Viterbo e l'Etruria Meridionale (esp. Dott. Zaccaria Mari), the Soprintendenza Speciale per i Beni Archeologici di Roma (esp. Arch. Giacomo Restante), and Dott.ssa Erminia Garofano. This research was supported by the Andrew W. Mellon Foundation through the Illinois Program for Research in the Humanities, the Italian Government, the late Dr. William and Mrs. Janet Gale, Macquarie University, the British Academy and British School at Rome, the Ed and Barbara Weil fund for Universal Biomineralization at the University of Illinois Urbana-Champaign and the National Aeronautics and Space Administration (NASA) Astrobiology Institute (Cooperative Agreement No. NNA13AA91A) issued through the Science Mission Directorate and the Chester and Helen Siess Professorship and the M.T. Geoffrey Yeh Chair in Civil and Environmental Engineering at the University of Illinois Urbana-Champaign. We also thank Julia Waldsmith and Megan Ward for assistance in the field and laboratory. Conclusions and interpretations presented in this study are those of the authors and do not necessarily reflect those of the funding agencies and permitting entities.

Author contributions

D.K.-J. contributed to conceptualization, funding acquisition, fieldwork and sample collection, data collection, data analysis, data curation, writing, submission, and review. D.M., M.H.G., and M.P. contributed to conceptualization, data analysis and curation, and writing, submission, and review. M.S. conducted the microscopy and contributed to data evaluation, and writing, submission, and review. R.K.S. contributed to data analysis, writing, submission, and review. B.W.F. contributed to conceptualization, funding acquisition, fieldwork and sample collection, data collection, data analysis, data curation, writing, submission, and review. All authors reviewed and read the manuscript and accepted this final submitted version. Conclusions in this study are those of the authors and do not necessarily reflect those of the funding or permitting agencies. Readers are welcome to comment on the online version of the paper. Correspondence should be addressed to D.K.-J. (d.keenanjones@uq.edu.au) and D.M. (davide.motta@northumbria.ac.uk). Information on materials and methods should be addressed to D.K.-J. (d.keenanjones@uq.edu.au).

Competing interests

The authors declare no competing interests.

Additional information

Supplementary Information The online version contains supplementary material available at <https://doi.org/10.1038/s41598-022-05158-2>.

Correspondence and requests for materials should be addressed to D.K.-J. or D.M.

Reprints and permissions information is available at www.nature.com/reprints.

Publisher's note Springer Nature remains neutral with regard to jurisdictional claims in published maps and institutional affiliations.



Open Access This article is licensed under a Creative Commons Attribution 4.0 International License, which permits use, sharing, adaptation, distribution and reproduction in any medium or format, as long as you give appropriate credit to the original author(s) and the source, provide a link to the Creative Commons licence, and indicate if changes were made. The images or other third party material in this article are included in the article's Creative Commons licence, unless indicated otherwise in a credit line to the material. If material is not included in the article's Creative Commons licence and your intended use is not permitted by statutory regulation or exceeds the permitted use, you will need to obtain permission directly from the copyright holder. To view a copy of this licence, visit <http://creativecommons.org/licenses/by/4.0/>.

© The Author(s) 2022